High-Entropy Alloys as Catalysts for the CO_2 and CO Reduction Reactions

Jack K. Pedersen[1], Thomas A.A. Batchelor[1], Alexander Bagger[1], and Jan Rossmeisl[1,*]

[1] *Department of Chemistry, University of Copenhagen, 2100 København Ø, Denmark*

[*] *Correspondence: jan.rossmeisl@chem.ku.dk*

September 16, 2019

Summary

Using the high-entropy alloys (HEAs) CoCuGaNiZn and AgAuCuPdPt as starting points we provide a framework for tuning the composition of disordered multi-metallic alloys to control the selectivity and activity of the reduction of carbon dioxide (CO_2) to highly reduced compounds. By combining density functional theory (DFT) with supervised machine learning we predicted the CO and hydrogen (H) adsorption energies of all surface sites on the (111) surface of the two HEAs. This allowed an optimization for the HEA compositions with increased likelihood for sites with weak hydrogen adsorption–to suppress the formation of molecular hydrogen (H_2)– and with strong CO adsorption to favor the reduction of CO. This led to the discovery of several disordered alloy catalyst candidates for which selectivity towards highly reduced carbon compounds is expected, as well as insights into the rational design of disordered alloy catalysts for the CO_2 and CO reduction reaction.

Introduction

The application of HEAs for catalytic purposes remains highly unexplored[1] but may provide the means of discovering new catalyst materials with better properties such as catalytic activity, selectivity, and stability by intelligently navigating the huge configuration space made possible by the vast number of combinations of elements in any ratio and their surface microstructures.[2]

So far HEAs (or equivalently, complex solid solutions and multi-principal-component alloys) have been studied experimentally for catalytic properties for the oxygen reduction[3–6] and evolution,[5,7] CO oxidation,[4] hydrogen evolution,[4,8] ammonia oxidation[9] and decomposition,[10] methanol oxidation,[4,6,11–14] and azo dye degradation[15] reactions.

The carbon dioxide reduction reaction (CO_2RR) and the subsequent carbon monoxide reduction reaction (CORR) have the potential to transform the production of carbon based fuels and commodity chemicals that is currently based on carbon from fossil sources into one based on a closed carbon cycle and therefore no net emissions of CO_2. One major obstacle with the large scale implementation of the electrochemical CO_2RR is the selective conversion of CO_2 into reduced products such as CO and formic acid (HCOOH), and highly reduced products such as methane (CH_4), methanol (CH_3OH), and ethene (CH_2CH_2). In aqueous environments one paramount challenge is to prevent the evolution of H_2, a competing electrochemical reaction which causes low faradaic efficiencies of the CO_2RR.[16]

The only pure metal surface that has shown the potential to form valuable, highly reduced carbon products beyond CO and formic acid is copper (Cu) albeit at a high overpotential.[17] It is thus natural that Cu has been investigated thoroughly to understand the properties that make this metal a unique catalyst in governing the CO_2RR selectivity. For instance, it has been shown that Cu has a close to optimal CO adsorption energy which accounts for the high activity and selectivity,[18,19] and that the adsorption energies of CO together with H are descriptors for the different product classes formed by various metal catalysts.[20,21] It was found that Cu is unique for the CO_2RR because it binds CO strongly enough to suppress the formation of CO and formic acid, and at the same time binds H weakly enough to suppress the formation of H_2. The strong binding of CO and the weak binding of H achieved by Cu thus seem to be necessary–but by no means sufficient–requirements for catalysts with selectivity towards highly reduced carbon products.

Unbiased searches for CO_2RR catalyst candidates have previously been performed,[22–24] however with an emphasis on binary alloys and without explicit regard to suppressing the evolution of H_2.

In this work we apply the catalytically promising multi-metallic HEAs as a basis for suggesting disordered alloy catalysts for the CO_2RR and tightly related CORR.

We recently showed that HEAs can act as a platform for the rational design of alloy catalysts for the oxygen reduction reaction by tuning the composition of the constituent elements to maximize the catalytic activity.[25] In this work we extend this methodology in an attempt to handle the more complex problem of controlling catalytic selectivity in the CO_2RR by using

the necessary requirements of having stronger CO binding and weaker H binding than Cu.[20]

CO and H adsorption energies are calculated on CoCuGaNiZn and AgAuCuPdPt

We chose the (111) facets of the face-centered cubic (fcc) HEAs CoCuGaNiZn and AgAuCuPdPt as the starting points for a composition optimization that will favor the selective reduction of CO_2 to highly reduced products. The elements in the two selected quinary HEAs are chosen to have both strong and weak adsorption strengths of CO and H, and at the same time span a popular selection of alloy catalysts in the literature of the CO_2RR (e.g. AgPd,[26,27] AuPd,[28,29] CuPd,[26,30] CuZn,[31] GaNi,[32] PdPt,[26,33] and AgAuCuPdPt[34]). Two quinary HEAs are chosen as opposed to one denary because the computational efforts in the following analysis increase rapidly with the number of elements. This means that one 5-parameter composition space is explored for each HEA and not the combination of the two.

A disordered surface comprised of many elements will naturally give rise to many different surface sites with distinct adsorption properties of the reaction intermediates of a given chemical reaction and will be determined by the microstructure of the site. Each site will contribute to the catalytic properties in a specific way determined to a large extent by the catalytic descriptors, in this case CO and H adsorption energies. The advantage that HEAs provide is a mean of probabilistically optimizing the catalytic properties for a given reaction by increasing the likelihood for surface microstructures with desired values of the adsorption energies.

Because of the vast number of possible surface microstructures the calculation of the adsorption energies for all possible adsorption sites is impossible even with the fastest ab initio simulations. Knowing the adsorption energies of all possible sites on the surface, however, it is possible to probabilistically evaluate the selectivity of a given alloy composition.

Herein, we shall overcome the constraint of calculating all available adsorption energies with the use of supervised machine learning. This allows the almost instantaneous prediction of the adsorption energies of all surface sites using only a subset of known DFT calculated adsorption energies and their corresponding surface structures as input for the machine learning regressor. It was found that Gaussian process regression (GPR), as implemented in scikit-learn,[35] generally gives the smallest prediction errors for both CO and H adsorption energies, and so this model is used in the following.

We assume in this work that CO adsorbs on-top and H in three-fold hollow sites, i.e. either fcc-hollow or hcp-hollow sites as illustrated in Figure S1. The data used to train the Gaussian

process regressors consist of hundreds of DFT adsorption energy calculations of on-top *CO, fcc H*, and hcp H*, respectively, for CoCuGaNiZn and AgAuCuPdPt, respectively, on randomly populated (111) facets of periodically repeated 2x2x5 slabs depicted in Figure S1. Details on the performed DFT calculations can be found in the section on the computational methods.

The adsorption site is described by the neighboring atoms

In order to train the GPR it must be fed a description of the surface microstructure which will make up the input of this machine learning model. Such an input can be chosen in many ways. To account for the ligand effect[36,37] in the surface microstructure we use the elemental labels of the atoms around an adsorption site (on-top or 3-fold hollow) as a categorical input. It is our hypothesis that the adsorption energy will be uniquely given by the elemental labels and locations relative to the adsorbate of all atoms in the system on a given surface. Fortunately, most of the chemical environment around the adsorption site is expected to depend only on the atoms in the immediate vicinity of the adsorbate, and in order to keep a cost-effective trade-off between computation time and accuracy we use as input only the closest spheres of neighbors as illustrated in Figure 1.

The generation of the input features follows our previously published outline,[25] and consists of the type of adsorption site, i.e. the metal atom adsorbing *CO on-top (5 possibilities) and the three metal atoms adsorbing H* in a hollow site (35 possibilities), together with the counts of the elemental labels of the atoms in the two nearest-neighbor spheres around the adsorbing atom(s) (210, 35, and 35 possibilities for the closest surface neighbors and 35, 35, and 5 for the closest subsurface neighbors for on-top, fcc-hollow, and hcp-hollow adsorption respectively). This is illustrated in Figure 1 for the three surface configurations of on-top, fcc-hollow, and hcp-hollow adsorption, giving rise to 15, 45, and 45 features in the input descriptions, respectively, and $5 \times 210 \times 35 = 36,750$; $35 \times 35 \times 35 = 42,875$; and $35 \times 35 \times 5 = 6,125$ distinct input descriptions, respectively. Examples of how to generate these are shown in Figure S3

The prediction of adsorption energies is successful

Feeding the GPR 80% of structures and their corresponding CO, fcc H, and hcp H DFT adsorption energies, and using the remaining 20% for validating the prediction accuracy in a five-fold cross-validation, yields mean absolute errors (MAEs) in the predictions of 63 and 43 meV, 51 and 65 meV, and 47 and 51 meV for CO, fcc H, and hcp H respectively on CoCuGaNiZn and

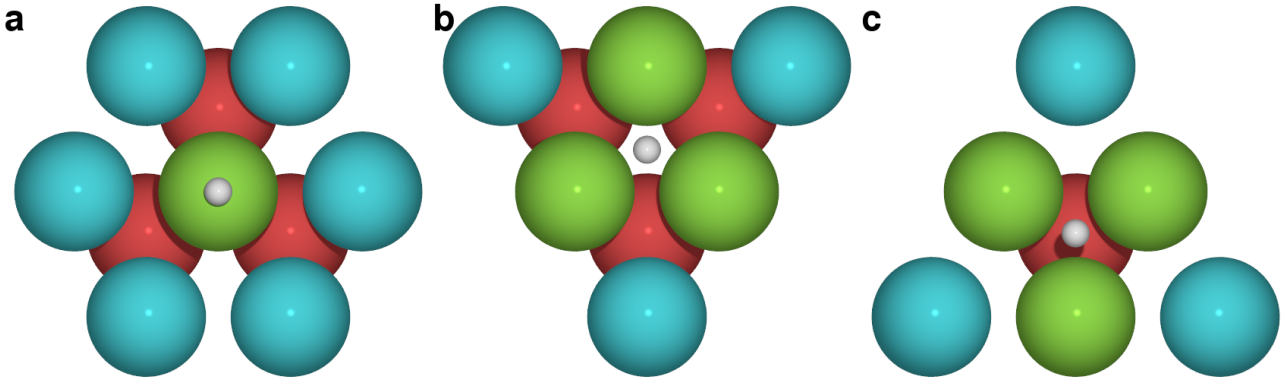

Figure 1: Adsorption site configurations.

Illustration of the neighboring atoms used to model the chemical environment around the surface site on a (111) surface for **(a)** on-top, **(b)** fcc-hollow, and **(c)** hcp-hollow adsorption. The white circles represent the adsorbing intermediate, green circles the adsorbing atoms on the surface, blue circles the closest surface neighbors, and red circles the closest subsurface neighbors.

AgAuCuPdPt respectively. This is illustrated in Figure 2 which shows the DFT calculated adsorption energies vs. the GPR predicted adsorption energies. The dotted lines represent a $\pm 0.1\,\mathrm{eV}$ deviation from the DFT values and as can be seen most predictions is within this boundary proving the GPR successful in capturing the most important parts of the chemical environment that influences the adsorption energy.

To evaluate the selectivity of the CO_2RR we develop a model in which the probability for weak adsorption of H* and strong adsorption of *CO are evaluated for each HEA composition. Setting the Cu H* and *CO adsorption energies, $\Delta E^{\mathrm{Cu}}_{\mathrm{H}^*}$ and $\Delta E^{\mathrm{Cu}}_{^*\mathrm{CO}}$, as the limits for overly weak H* binding and overly strong *CO binding respectively, we can define a measure of the CO_2RR selectivity as the probability of surface sites with weaker H* binding than Cu. Similarly a measure of the CORR activity can be defined as the joint, independent probability of surface sites with weaker H* binding than Cu *and* stronger *CO binding than Cu.

Using the predicted adsorption energies obtained with GPR and the probability for each surface microstructure given by

$$P_i(\mathbf{f}) = \prod_{k=1}^{M} f_k^{n_{ik}},$$

it is possible to produce the activity-selectivity maps shown in Figure 3. Here, P_i is the probability of the surface microstructure labeled i, $\mathbf{f}$ is the vector of molar fractions for each element, M is the number of metals in the HEA, f_k is the molar fraction of element k, and n_{ik} is the number of element k in the surface microstructure labeled i.

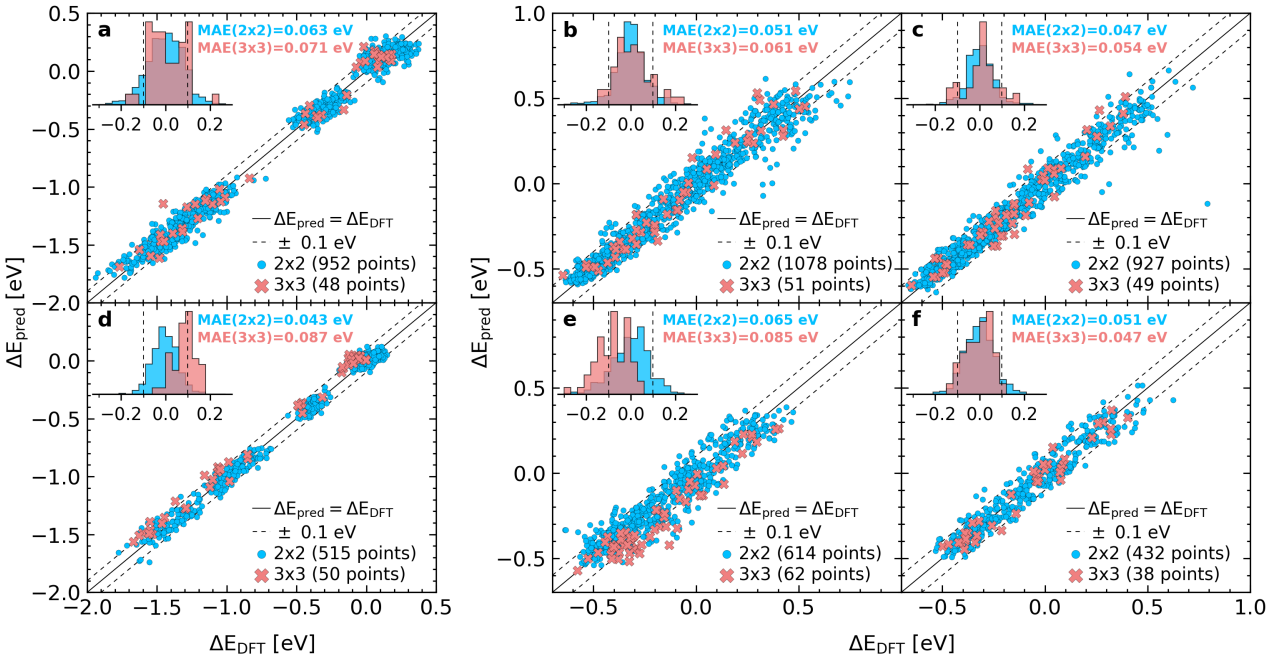

Figure 2: Predicted vs. calculated adsorption energies.

Plots showing the GPR predicted vs. the DFT calculated adsorption energies for CoCuGaNiZn (**a-c**) and AgAuCuPdPt (**d-f**) for on-top *CO (**a,d**), fcc-hollow H* (**b,e**), and hcp-hollow H* (**c,f**). Blue indicates data for 2x2 slabs and red 3x3 slabs. The mean absolute errors (MEAs) are calculated as a 5-fold cross-validation prediction error for the 2x2 slabs, and for the 3x3 slabs as the prediction error when training on the set of all 2x2 slabs. The insets show the distribution of the prediction errors in eV defined as $\Delta E_{pred} - \Delta E_{DFT}$.

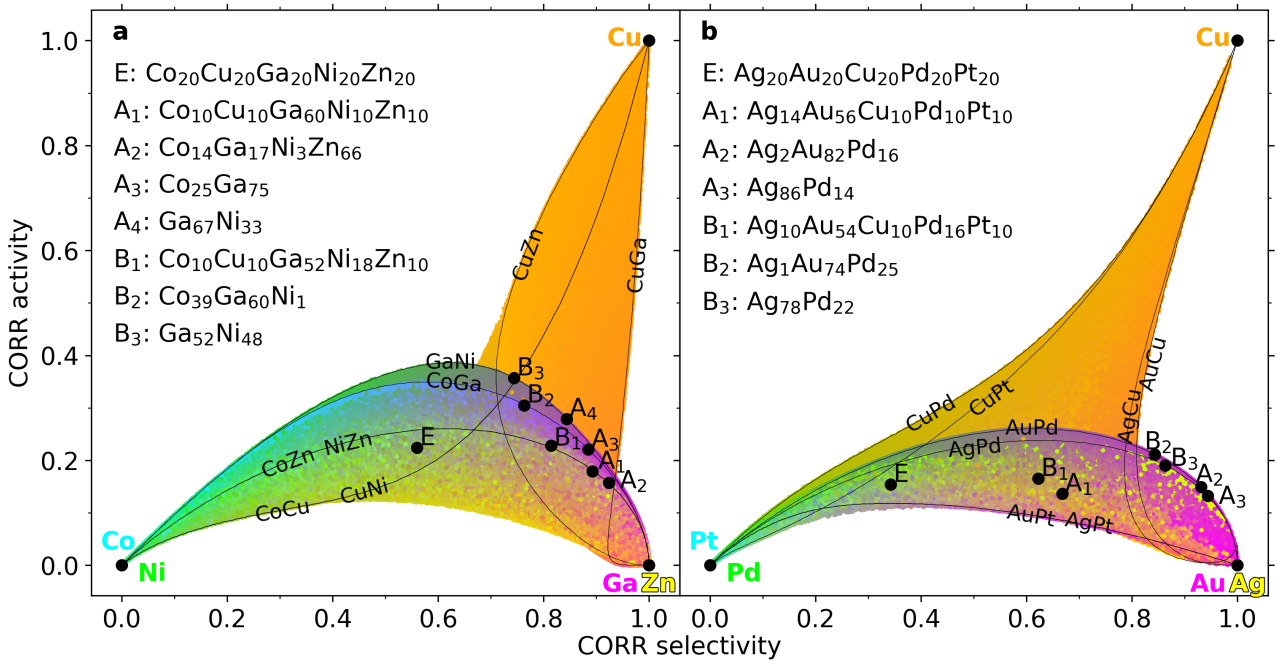

Figure 3: Activity-selectivity plots.

Plot of the CORR selectivity and CORR activity spaces achievable by CoCuGaNiZn **(a)** and AgAuCuPdPt **(b)**. Here, CORR selectivity (x) is defined as the proportion of sites with $\Delta E_{\mathrm{H}^*} \geq \Delta E_{\mathrm{H}^*}^{\mathrm{Cu}}$ and CORR activity (y) as the proportion of sites with $\Delta E_{\mathrm{H}^*} \geq \Delta E_{\mathrm{H}^*}^{\mathrm{Cu}}$ times the proportion of sites with $\Delta E_{*\mathrm{CO}} \leq \Delta E_{*\mathrm{CO}}^{\mathrm{Cu}}$. Every point represents a composition of the HEAs and the colors indicate the ratios (e.g. Cu-rich compositions being orange). The solid black lines represent the achievable spaces spanned by binary alloys as labeled. Locally optimal compositions obtained when optimizing $x + y$ and $x + 2y$ respectively are shown labeled $\mathrm{A_i}$ and $\mathrm{B_i}$, as well as the pure elements and the equimolar composition, E.

The plots in Figure 3 show how the selectivity and activity of the CO_2RR and the subsequent reduction of CO is expected to change as the HEA catalysts vary in composition according to our model. The colored areas show the space of CO_2RR selectivities and CORR activities within which can be navigated by tuning the compositions of the HEAs. It is seen that most of the achievable space of selectivity and activity is bounded by the traces of the binary alloys. This means that an optimization of the composition to give the highest selectivity and activity can be expected to yield mainly binary alloys. It is also seen that moving towards the upper right corner, corresponding to optimal selectivity towards highly reduced carbon products, will yield Cu as the optimal catalyst by construction.

With some given trade-off between CO_2RR selectivity (x) and CORR activity (y) we can list locally optimal compositions of the HEAs for which a slight change in the molar fractions do not produce a better trade-off using an in-house optimization algorithm. If, for instance, CO_2RR selectivity and CORR activity are weighted equally, corresponding to maximizing the sum $x+y$, locally optimal compositions are: Cu (2.00), $Ga_{67}Ni_{33}$ (1.12), $Co_{25}Ga_{75}$ (1.11), $Co_{14}Ga_{17}Ni_3Zn_{66}$ (1.08), $Ag_2Au_{82}Pd_{16}$ (1.08), and $Ag_{86}Pd_{14}$ (1.08), where the numbers in parentheses are the sums $x + y$ for the given molar fraction. These locally optimal compositions are shown as subscripted A's in Figure 3.

However, constraints on the composition can also be applied on top of this to ensure HEAs containing all five metals at near-equimolar ratios so that the assumption of a disordered solid solution phase is expected to hold. For instance, as shown in Figure 3, optimizing under a constraint of a minimum of 10% of each element results in the HEAs $Co_{10}Cu_{10}Ga_{60}Ni_{10}Zn_{10}$ (1.07) and $Ag_{14}Au_{56}Cu_{10}Pd_{10}Pt_{10}$ (0.81) with only some reduction in CO_2RR selectivity and CORR activity compared to the best alloy alternatives.

Other trade-offs between CO_2RR selectivity and CORR activity can be selected to obtain different HEAs. In Figure 3 are shown some local optima for the case where CORR activity has twice the weight of CO_2RR selectivity labeled with subscripted B's.

By inspection of the selectivity-activity maps in Figure 3, and the preceding composition optimization, this model has allowed an unbiased discovery of new catalyst candidates using only the knowledge about the catalytic selectivity and adsorption properties of Cu. For instance, GaNi alloys in various ratios are expected from this model to show superior ability to reduce CO to highly reduced carbon products compared to other disordered alloy combinations, since it forms the upper boundary of the achievable selectivity-activity space of non-copper alloys in Figure 3**a**. Indeed, GaNi alloys have been shown to have some selectivity towards highly reduced carbon products in experiments.[32]

Every set of molar fractions, and thus every point in Figure 3, has a corresponding distinct distribution of H and CO adsorption energies. Examples of these distributions are shown in Figure 4, for six representative alloy compositions. Figure 4 also provides a graphical way of interpreting the CO_2RR selectivity as the probability of having sites to the right of the vertical H adsorption line defined by Cu(111), and the CORR activity as the probability of having sites in the lower right quadrant defined by the H and CO adsorption lines for Cu(111).

Figure 4 illustrates how tuning the compositions of the disordered alloys can alter the distribution of adsorption energies, and thus change the selectivity and activity of the disordered alloys. As shown in Figure 4**c** and **f**, the sites whose likelihood are increased during the optimization of the composition are 3-fold hollow sites with weak H adsorption (e.g. GaGaGa, GaGaNi, AuAuAu, and AuAuPd) and on-top sites with strong CO adsorption (Ni and Pd). One way to interpret the factors that determine the optimal compositions is thus a trade-off between strong CO adsorbing elements that both in numbers and through the ligand effect cause the weakest possible adsorption of H. The superior ability of alloying with Ga compared to the other elements that adsorb CO weakly (i.e. Zn, Ag, Au) thus seem to be related to a perturbation that weakens the adsorption of H in 3-fold hollow sites where strong H adsorbing elements (i.e. Co and Ni) are present.

Conclusion

We have presented a framework for the unbiased discovery of new catalyst candidates for the CORR using the two disordered HEAs CoCuGaNiZn and AgAuCuPdPt as starting points. Using the necessary –but by no means sufficient– criteria of weak H adsorption and strong CO adsorption we predict locally optimal disordered alloy compositions as shown in Figure 3 and simultaneously provide an understanding of how affecting the distribution of adsorption energies by tuning the composition impacts the affinity for H_2 formation and CO reduction.

Knowing only the catalytic properties of Cu the model is able to suggest, for instance, GaNi as a locally optimal catalyst candidate for the CORR, which is known experimentally to show some affinity towards highly reduced carbon products.[32] This demonstrates the model's ability to predict valid candidates without prior knowledge of their catalytic properties.

Computational methods

All calculation were performed with DFT with the RPBE[38] functional using the Atomistic Simulation Environment (ASE)[39] and the GPAW code[40,41] using a plane-wave expansion of the

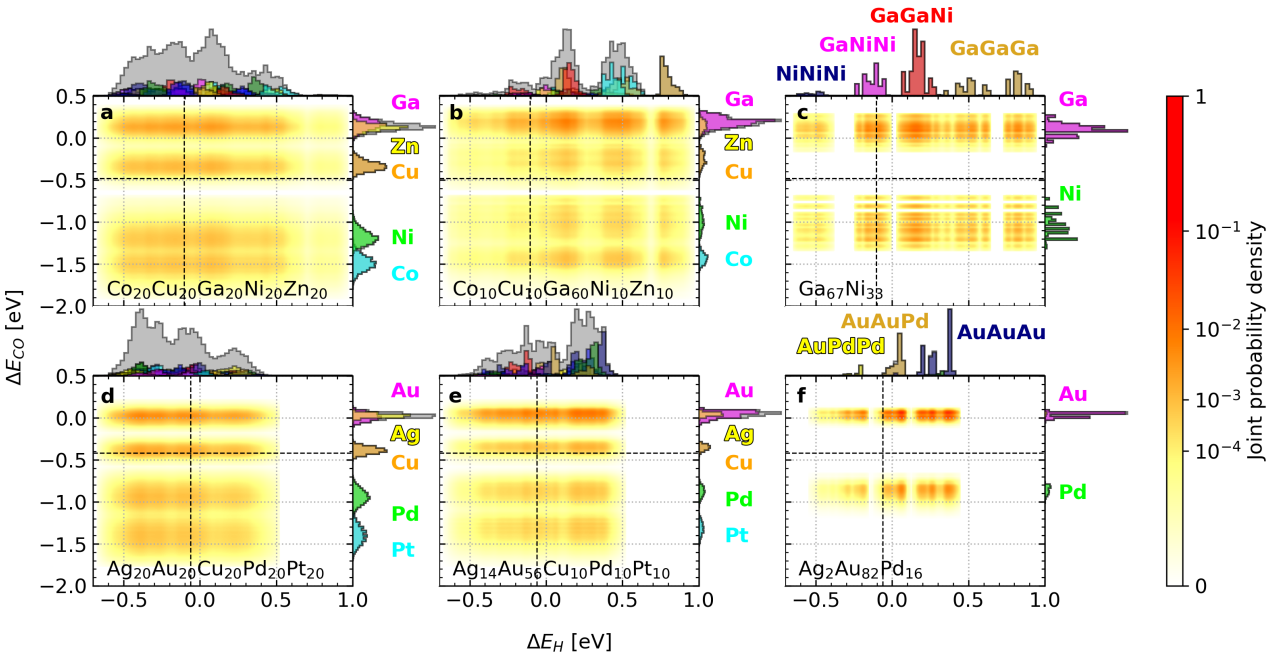

Figure 4: Adsorption energy distributions.

Plot of the distributions of H* and *CO adsorption energies for six disordered (111) alloys using as starting point CoCuGaNiZn (**a-c**) and AgAuCuPdPt (**d-f**) showing equimolar compositions (**a,d**), optimal compositions with a minimum of 10% of each element (**b,e**), and locally optimal compositions without constraints (**c,f**). The histograms on the axes show the distributions of H* and *CO adsorption energies with colors indicating the adsorption sites as indicated for a selection of peaks on a gray background that represents the total distribution of all adsorption sites. The square plots show the joint, independent distributions of H* and *CO adsorption energies with probability indicated by the colorbar. The dashed black lines show the adsorption energies of Cu as predicted by the regressors.

wavefunction.

Adsorption energies were calculated on planar periodic 2x2x5 slabs and 3x3x5 slabs illustrated in Figure S1 with a plane-wave cutoff at 400 eV and a Monhorst-Pack k-point sampling of the Brillouin zone of (4,4,1) for CoCuGaNiZn and (8,8,1) for AgAuCuPdPt. The slabs were relaxed to a maximum force of 0.1 eV/Å on the atoms and in the case of CoCuGaNiZn the calculations were performed with spin polarized orbitals. A 10 Å layer of vacuum was added on the top and bottom of the slab and the positions of the atoms where fixed for all but the two top layers which were allowed to relax. The energy of the gas phase reference molecules CO and H_2 were calculated in identical super cells and with the same DFT parameters as for the slabs. The adsorption energies of CO and H were calculated as

$$\Delta E_{*\mathrm{CO}} = E_{*\mathrm{CO}} - E_{*} - E_{\mathrm{CO}} \tag{1}$$

$$\Delta E_{\mathrm{H}^*} = E_{\mathrm{H}^*} - E_{*} - \frac{1}{2}E_{\mathrm{H_2}} \tag{2}$$

where $\Delta E_{*\mathrm{CO}}$ and ΔE_{H^*} are the adsorption energies of CO and H, $E_{*\mathrm{CO}}$ and E_{H^*} are the DFT energies of the relaxed slabs with the adsorbate, E_* is the DFT energy of the slab without any adsorbate, and E_{CO} and $E_{\mathrm{H_2}}$ are the DFT energies of the molecular gas phase references.

The lattice parameter for the slabs was chosen as the weighted average of the DFT calculated lattice parameters of the constituent elements in the top layer of the slab. We expect this lattice parameter to most accurately account for the effect of strain on a real HEA surface.

The lattice parameters corresponding to a minimum in energy of the individual elements listed in Table S1 were calculated for a primitive fcc unit cell with a plane-wave cutoff of 400 eV and a Monkhorst-Pack k-points sampling of (14,14,14) with spin-polarized orbitals for Co and Ni, and spin-paired orbitals for the other elements.

Keywords

Electrocatalysis, CO_2 reduction reaction, CO reduction reaction, high-entropy alloy, multicomponent alloy, complex solid solution, rational design, adsorption energy prediction.

Author contributions

J.P. wrote the paper and carried out the DFT calculations and the modeling. J.P., T.B. and J.R. provided the conceptual framework of the methodology, and A.B. and J.R. guided the project.

Declaration of interests

The authors declare no competing interests.

References

[1] Löffler, T., Savan, A., Garzón-Manjón, A., Meischein, M., Scheu, C., Ludwig, A., and Schuhmann, W. (2019). Toward a Paradigm Shift in Electrocatalysis Using Complex Solid Solution Nanoparticles. ACS Energy Letters *4*, 1206–1214. https://doi.org/10.1021/acsenergylett.9b00531.

[2] Ludwig, A. (2019). Discovery of new materials using combinatorial synthesis and high-throughput characterization of thin-film materials libraries combined with computational methods. npj Computational Materials *5*, 70. https://doi.org/10.1038/s41524-019-0205-0.

[3] Löffler, T., Meyer, H., Savan, A., Wilde, P., Garzón Manjón, A., Chen, Y.-T., Ventosa, E., Scheu, C., Ludwig, A., and Schuhmann, W. (2018). Discovery of a Multinary Noble Metal-Free Oxygen Reduction Catalyst. Advanced Energy Materials *8*, 1802269. https://doi.org/10.1002/aenm.201802269.

[4] Qiu, H.-J., Fang, G., Wen, Y., Liu, P., Xie, G., Liu, X., and Sun, S. (2019). Nanoporous high-entropy alloys for highly stable and efficient catalysts. J. Mater. Chem. A *7*, 6499–6506. https://doi.org/10.1039/C9TA00505F.

[5] Lacey, S. D., Dong, Q., Huang, Z., Luo, J., Xie, H., Lin, Z., Kirsch, D. J., Vattipalli, V., Povinelli, C., Fan, W., et al. (2019). Stable Multimetallic Nanoparticles for Oxygen Electrocatalysis. Nano Letters https://doi.org/10.1021/acs.nanolett.9b01523.

[6] Chen, X., Si, C., Gao, Y., Frenzel, J., Sun, J., Eggeler, G., and Zhang, Z. (2015). Multi-component nanoporous platinum–ruthenium–copper–osmium–iridium alloy with enhanced electrocatalytic activity towards methanol oxidation and oxygen reduction. Journal of Power Sources *273*, 324 – 332. https://doi.org/10.1016/j.jpowsour.2014.09.076.

[7] Glasscott, M. W., Pendergast, A. D., Goines, S., Bishop, A. R., Hoang, A. T., Renault, C., and Dick, J. E. (2019). Electrosynthesis of high-entropy metallic glass nanoparticles for designer, multi-functional electrocatalysis. Nature Communications *10*, 2650. https://doi.org/10.1038/s41467-019-10303-z.

[8] Zhang, G., Ming, K., Kang, J., Huang, Q., Zhang, Z., Zheng, X., and Bi, X. (2018). High entropy alloy as a highly active and stable electrocatalyst for hydrogen evolution reaction. Electrochimica Acta *279*, 19 – 23. https://doi.org/10.1016/j.electacta.2018.05.035.

[9] Yao, Y., Huang, Z., Xie, P., Lacey, S. D., Jacob, R. J., Xie, H., Chen, F., Nie, A., Pu, T., Rehwoldt, M., et al. (2018). Carbothermal shock synthesis of high-entropy-alloy nanoparticles. Science *359*, 1489–1494. https://doi.org/10.1126/science.aan5412.

[10] Xie, P., Yao, Y., Huang, Z., Liu, Z., Zhang, J., Li, T., Wang, G., Shahbazian-Yassar, R., Hu, L., and Wang, C. (2019). Highly efficient decomposition of ammonia using high-entropy alloy catalysts. Nature Communications *10*, 4011. https://doi.org/10.1038/s41467-019-11848-9.

[11] Yusenko, K. V., Riva, S., Carvalho, P. A., Yusenko, M. V., Arnaboldi, S., Sukhikh, A. S., Hanfland, M., and Gromilov, S. A. (2017). First hexagonal close packed high-entropy alloy with outstanding stability under extreme conditions and electrocatalytic activity for methanol oxidation. Scripta Materialia *138*, 22 – 27. https://doi.org/10.1016/j.scriptamat.2017.05.022.

[12] Tsai, C.-F., Wu, P.-W., Lin, P., Chao, C.-G., and Yeh, K.-Y. (2008). Sputter Deposition of Multi-Element Nanoparticles as Electrocatalysts for Methanol Oxidation. Japanese Journal of Applied Physics *47*, 5755–5761. https://doi.org/10.1143/jjap.47.5755.

[13] Tsai, C.-F., Yeh, K.-Y., Wu, P.-W., Hsieh, Y.-F., and Lin, P. (2009). Effect of platinum present in multi-element nanoparticles on methanol oxidation. Journal of Alloys and Compounds *478*, 868 – 871. https://doi.org/10.1016/j.jallcom.2008.12.055.

[14] Wang, A.-L., Wan, H.-C., Xu, H., Tong, Y.-X., and Li, G.-R. (2014). Quinary PdNiCoCuFe Alloy Nanotube Arrays as Efficient Electrocatalysts for Methanol Oxidation. Electrochimica Acta *127*, 448 – 453. https://doi.org/10.1016/j.electacta.2014.02.076.

[15] Lv, Z. Y., Liu, X. J., Jia, B., Wang, H., Wu, Y., and Lu, Z. P. (2016). Development of a novel high-entropy alloy with eminent efficiency of degrading azo dye solutions. Scientific Reports *6*, 34213. https://doi.org/10.1038/srep34213.

[16] Khezri, B., Fisher, A. C., and Pumera, M. (2017). CO2 reduction: the quest for electrocatalytic materials. J. Mater. Chem. A *5*, 8230–8246. https://doi.org/10.1039/C6TA09875D.

[17] Hori, Y., Wakebe, H., Tsukamoto, T., and Koga, O. (1994). Electrocatalytic process of CO selectivity in electrochemical reduction of CO2 at metal electrodes in aqueous media. Electrochimica Acta *39*, 1833 – 1839. https://doi.org/10.1016/0013-4686(94)85172-7.

[18] Liu, X., Xiao, J., Peng, H., Hong, X., Chan, K., and Nørskov, J. K. (2017). Understanding trends in electrochemical carbon dioxide reduction rates. Nature Communications *8*. https://doi.org/10.1038/ncomms15438.

[19] Peterson, A. A. and Nørskov, J. K. (2012). Activity Descriptors for CO2 Electroreduction to Methane on Transition-Metal Catalysts. The Journal of Physical Chemistry Letters *3*, 251–258. https://doi.org/10.1021/jz201461p.

[20] Bagger, A., Ju, W., Varela, A. S., Strasser, P., and Rossmeisl, J. (2017). Electrochemical CO2 Reduction: A Classification Problem. ChemPhysChem *18*, 3266–3273. https://doi.org/10.1002/cphc.201700736.

[21] Hussain, J., Jónsson, H., and Skúlason, E. (2018). Calculations of Product Selectivity in Electrochemical CO2 Reduction. ACS Catalysis *8*, 5240–5249. https://doi.org/10.1021/acscatal.7b03308.

[22] Ma, X., Li, Z., Achenie, L. E. K., and Xin, H. (2015). Machine-Learning-Augmented Chemisorption Model for CO2 Electroreduction Catalyst Screening. The Journal of Physical Chemistry Letters *6*, 3528–3533. https://doi.org/10.1021/acs.jpclett.5b01660.

[23] Ulissi, Z. W., Tang, M. T., Xiao, J., Liu, X., Torelli, D. A., Karamad, M., Cummins, K., Hahn, C., Lewis, N. S., Jaramillo, T. F., et al. (2017). Machine-Learning Methods Enable Exhaustive Searches for Active Bimetallic Facets and Reveal Active Site Motifs for CO2 Reduction. ACS Catalysis *7*, 6600–6608. https://doi.org/10.1021/acscatal.7b01648.

[24] Tran, K. and Ulissi, Z. W. (2018). Active learning across intermetallics to guide discovery of electrocatalysts for CO2 reduction and H2 evolution. Nature Catalysis *1*, 696 – 703. https://doi.org/10.1038/s41929-018-0142-1.

[25] Batchelor, T. A., Pedersen, J. K., Winther, S. H., Castelli, I. E., Jacobsen, K. W., and Rossmeisl, J. (2019). High-Entropy Alloys as a Discovery Platform for Electrocatalysis. Joule *3*, 834 – 845. https://doi.org/10.1016/j.joule.2018.12.015.

[26] Lee, J. H., Kattel, S., Jiang, Z., Xie, Z., Yao, S., Tackett, B. M., Xu, W., Marinkovic, N. S., and Chen, J. G. (2019). Tuning the activity and selectivity of electroreduction of CO2 to synthesis gas using bimetallic catalysts. Nature Communications *10*, 3724. https://doi.org/10.1038/s41467-019-11352-0.

[27] Zeng, J., Zhang, W., Yang, Y., Li, D., Yu, X., and Gao, Q. (2019). Pd–Ag Alloy Electrocatalysts for CO2 Reduction: Composition Tuning to Break the Scaling Relationship. ACS Applied Materials & Interfaces *11*, 33074–33081. https://doi.org/10.1021/acsami.9b11729.

[28] Hahn, C., Abram, D. N., Hansen, H. A., Hatsukade, T., Jackson, A., Johnson, N. C., Hellstern, T. R., Kuhl, K. P., Cave, E. R., Feaster, J. T., et al. (2015). Synthesis of thin film AuPd alloys and their investigation for electrocatalytic CO2 reduction. J. Mater. Chem. A *3*, 20185–20194. http://doi.org/10.1039/C5TA04863J.

[29] Kortlever, R., Peters, I., Balemans, C., Kas, R., Kwon, Y., Mul, G., and Koper, M. T. M. (2016). Palladium–gold catalyst for the electrochemical reduction of CO2 to C1–C5 hydrocarbons. Chem. Commun. *52*, 10229–10232. https://doi.org/10.1039/C6CC03717H.

[30] Ma, S., Sadakiyo, M., Heima, M., Luo, R., Haasch, R. T., Gold, J. I., Yamauchi, M., and Kenis, P. J. A. (2017). Electroreduction of Carbon Dioxide to Hydrocarbons Using Bimetallic Cu–Pd Catalysts with Different Mixing Patterns. Journal of the American Chemical Society *139*, 47–50. https://doi.org/10.1021/jacs.6b10740.

[31] Feng, Y., Li, Z., Liu, H., Dong, C., Wang, J., Kulinich, S. A., and Du, X. (2018). Laser-Prepared CuZn Alloy Catalyst for Selective Electrochemical Reduction of CO2 to Ethylene. Langmuir *34*, 13544–13549. https://doi.org/10.1021/acs.langmuir.8b02837.

[32] Torelli, D. A., Francis, S. A., Crompton, J. C., Javier, A., Thompson, J. R., Brunschwig, B. S., Soriaga, M. P., and Lewis, N. S. (2016). Nickel-Gallium-Catalyzed Electrochemical Reduction of CO2 to Highly Reduced Products at Low Overpotentials. ACS Catalysis *6*, 2100–2104. https://doi.org/10.1021/acscatal.5b02888.

[33] Kortlever, R., Peters, I., Koper, S., and Koper, M. T. M. (2015). Electrochemical CO2 Reduction to Formic Acid at Low Overpotential and with High Faradaic Efficiency on Carbon-Supported Bimetallic Pd–Pt Nanoparticles. ACS Catalysis *5*, 3916–3923. https://doi.org/10.1021/acscatal.5b00602.

[34] Nellaiappan, S., Kumar, N., Kumar, R., Parui, A., Malviya, K. D., Pradeep, K. G., Singh, A. K., Sharma, S., Tiwary, C. S., and Biswas, K. (2019). Nobel Metal Based High Entropy Alloy for Conversion of Carbon Dioxide (CO2) to Hydrocarbon https://doi.org/10.26434/chemrxiv.9777218.v1.

[35] Pedregosa, F., Varoquaux, G., Gramfort, A., Michel, V., Thirion, B., Grisel, O., Blondel, M., Prettenhofer, P., Weiss, R., Dubourg, V., et al. (2011). Scikit-learn: Machine Learning in Python. Journal of Machine Learning Research *12*, 2825–2830. http://www.jmlr.org/papers/v12/pedregosa11a.html.

[36] Kitchin, J. R., Nørskov, J. K., Barteau, M. A., and Chen, J. G. (2004). Role of Strain and Ligand Effects in the Modification of the Electronic and Chemical Properties of Bimetallic Surfaces. Phys. Rev. Lett. *93*, 156801. https://doi.org/10.1103/PhysRevLett.93.156801.

[37] Escudero-Escribano, M., Verdaguer-Casadevall, A., Malacrida, P., Grønbjerg, U., Knudsen, B. P., Jepsen, A. K., Rossmeisl, J., Stephens, I. E. L., and Chorkendorff, I. (2012). Pt5Gd as a Highly Active and Stable Catalyst for Oxygen Electroreduction. Journal of the American Chemical Society *134*, 16476–16479. https://doi.org/10.1021/ja306348d.

[38] Hammer, B., Hansen, L. B., and Nørskov, J. K. (1999). Improved Adsorption Energetics within Density-Functional Theory Using Revised Perdew-Burke-Ernzerhof Functionals. Physical Review B *59*, 7413–7421. https://doi.org/10.1103/PhysRevB.59.7413.

[39] Larsen, A. H., Mortensen, J. J., Blomqvist, J., Castelli, I. E., Christensen, R., Dułak, M., Friis, J., Groves, M. N., Hammer, B., Hargus, C., et al. (2017). The atomic simulation environment—a Python library for working with atoms. Journal of Physics: Condensed Matter *29*, 273002. https://doi.org/10.1088/1361-648X/aa680e.

[40] Mortensen, J. J., Hansen, L. B., and Jacobsen, K. W. (2005). Real-space grid implementation of the projector augmented wave method. Physical Review B *71*, 035109. https://link.aps.org/doi/10.1103/PhysRevB.71.035109.

[41] Enkovaara, J., Rostgaard, C., Mortensen, J. J., Chen, J., Dułak, M., Ferrighi, L., Gavnholt, J., Glinsvad, C., Haikola, V., Hansen, H. A., et al. (2010). Electronic structure calculations with GPAW: a real-space implementation of the projector augmented-wave method. Journal of Physics: Condensed Matter *22*, 253202. https://doi.org/10.1088/0953-8984/22/25/253202.